The Astrophysical Journal, 720:114–129, 2010 September 1 doi:10.1088/0004-637X/720/1/114

MID-INFRARED PHOTOMETRIC ANALYSIS OF MAIN BELT ASTEROIDS: A TECHNIQUE FOR COLOR–COLOR DIFFERENTIATION FROM BACKGROUND ASTROPHYSICAL SOURCES

B. Bhattacharya[1], A. Noriega-Crespo[2], B. E. Penprase[3], V. S. Meadows[4], M. Salvato[5,6], H. Aussel[7], D. Frayer[8], O. Ilbert[9], E. Le Floc'h[9], D. Looper[9], J. Surace[2], P. Capak[2], J. D. Giorgini[10], M. Granvik[9], C. Grillmair[2], A. Hagen[11], G. Helou[1,2,5], W. T. Reach[12], L. M. Rebull[2], D. B. Sanders[9], N. Scoville[5], K. Sheth[13], and L. Yan[14]

[1] NASA Herschel Science Center, California Institute of Technology, MC 100-22, Pasadena, CA 91125, USA
[2] Spitzer Science Center, California Institute of Technology, Pasadena, CA 91125, USA
[3] Department of Physics and Astronomy, Pomona College, Claremont, CA 91711, USA
[4] Department of Astronomy, University of Washington, Seattle, WA 98195, USA
[5] Department of Astronomy, California Institute of Technology, Pasadena, CA 91125, USA
[6] Max Planck Institute for Plasma Physics and Cluster of Excellence, Garching, Germany
[7] Service d'Astrophysique, CEA/Saclay, Gif-sur-Yvette, France
[8] NRAO, NRAO, Green Bank, WV 24944, USA
[9] Institute for Astronomy, University of Hawaii, Honolulu, HI 96822, USA
[10] Jet Propulsion Laboratory, California Institute of Technology, Pasadena, CA 91109, USA
[11] Department of Physics, Harvey Mudd College, Claremont, CA 91711, USA
[12] Stratospheric Observatory for Infrared Astronomy, Universities Space Research Association, NASA Ames Research Center, Mail Stop 211-3, Moffett Field, CA 94035
[13] NRAO/NAASC, Charlottesville, VA 22903, USA
[14] WISE Data Center, California Institute of Technology, Pasadena, CA 91125, USA
Received 2009 May 12; accepted 2010 June 16; published 2010 August 6

ABSTRACT

The *Spitzer Space Telescope* routinely detects asteroids in astrophysical observations near the ecliptic plane. For the galactic or extragalactic astronomer, these solar system bodies can introduce appreciable uncertainty into the source identification process. We discuss an infrared color discrimination tool that may be used to distinguish between solar system objects and extrasolar sources. We employ four *Spitzer* Legacy data sets, the First Look Survey-Ecliptic Plane Component (FLS-EPC), SCOSMOS, SWIRE, and GOODS. We use the Standard Thermal Model to derive FLS-EPC main belt asteroid (MBA) diameters of 1–4 km for the numbered asteroids in our sample and note that several of our solar system sources may have fainter absolute magnitude values than previously thought. A number of the MBAs are detected at flux densities as low as a few tens of μJy at 3.6 μm. As the FLS-EPC provides the only 3.6–24.0 μm observations of individual asteroids to date, we are able to use this data set to carry out a detailed study of asteroid color in comparison to astrophysical sources observed by SCOSMOS, SWIRE, and GOODS. Both SCOSMOS and SWIRE have identified a significant number of asteroids in their data, and we investigate the effectiveness of using relative color to distinguish between asteroids and background objects. We find a notable difference in color in the IRAC 3.6–8.0 mm and MIPS 24 μm bands between the majority of MBAs, stars, galaxies, and active galactic nuclei, though this variation is less significant when comparing fluxes in individual bands. We find median colors for the FLS-EPC asteroids to be $[F(5.8/3.6), F(8.0/4.5), F(24/8)] = (4.9\pm1.8, 8.9\pm7.4, 6.4\pm2.3)$. Finally, we consider the utility of this technique for other mid-infrared observations that are sensitive to near-Earth objects, MBAs, and trans-Neptunian objects. We consider the potential of using color to differentiate between solar system and background sources for several space-based observatories, including Warm *Spitzer*, *Herschel*, and *WISE*.

Key words: minor planets, asteroids: general – techniques: photometric

1. INTRODUCTION

Asteroids are remnants of the early solar system and provide clues to its origin and evolution. Unlike planets and satellites, they are not subject to appreciable geological evolution, have remained relatively pristine since their formation, and can provide insight into the primordial solar nebula. Their current surface characteristics and size distributions serve as markers of the physical and orbital evolution and of the effects of long-term space weathering on objects within our solar system. As asteroids are routinely present in *Spitzer Space Telescope* observations near the ecliptic plane, characterizing their prevalence as a function of ecliptic latitude is of interest to the larger astronomical community.

The solar system's main belt asteroid (MBA) population can be characterized through the definition of size frequency distributions (SFDs), taxonomies, and surface properties. To date, this work has been carried out using primarily ground-based data. Models such as Tedesco et al.'s (2005) must extrapolate the accurate distribution functions for larger MBAs to derive properties for smaller asteroids with diameters of $\sim$1 km. Ground-based discovery surveys, because they detect reflected sunlight rather than thermal emission at optical wavelengths, are constrained to detect higher albedo, larger asteroids.

Since the launch of NASA's last Great Observatory, the *Spitzer Space Telescope*, mid-infrared measurements have provided a detailed look at the $\sim$1 km MBA population. *Spitzer* is highly sensitive and measures thermal emission from previously undetected, small asteroids, whose peak thermal flux is emitted in or near the Infrared Array Camera (IRAC; Fazio et al. 2004)) and Multiband Imaging Photometer for *Spitzer* (MIPS; Rieke et al. 2004) bandpasses, as seen in Figure 1, where a typical MBA spectral energy distribution (SED) is given, along with measured FLS-EPC fluxes for six asteroids. The detected asteroid flux is dual-peaked, and reflected sunlight at optical wavelengths is often a factor of $\sim10^3$ below the thermal Wien

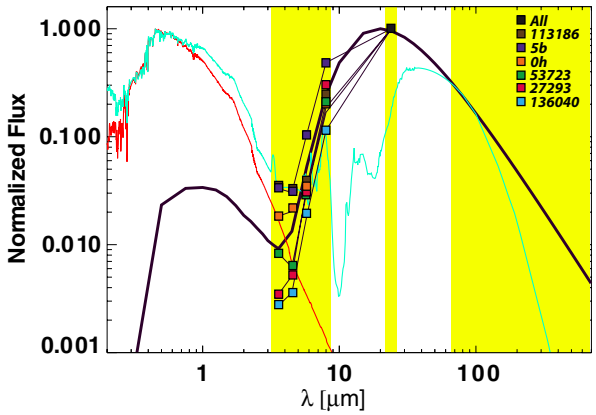

Figure 1. Modeled SED for a typical S-type MBA. This model considers both reflected sunlight and thermal emission, as described by the STM (black solid line; Lebofsky & Spencer 1989). The shaded areas, from left to right, indicate the *Spitzer* IRAC 3.6–8 μm, MIPS 24 μm, and *Herschel* PACS 55–210 μm bandpasses. Note the marked increase in flux from this asteroid ($p_v = 0.23$) at thermal wavelengths. Overlaid as lines are template SEDs for a ULIRG (Arp220; cyan color) and for an elliptical galaxy (red). The cyan line is dual peaked, with the left peak representing star light and the secondary, far-infrared peak indicative of stellar emission that has been absorbed by dust and re-emitted thermally. The central features include absorption by silicate dust and emission by polycyclic aromatic hydrocarbons (PAHs). A stellar SED would be comparable to that of the elliptical galaxy shown here. The squares represented measured FLS-EPC asteroid flux in the IRAC and MIPS 24 μm bandpasses. At *Spitzer* wavelengths, where asteroid flux is increasing, extrasolar sources exhibit a drop in flux, or at least a smaller increase flux than asteroids. This allows for color differentiation between the different classes of objects when time-separated data are not available.

peak. For MBAs, while thermal flux is detected by the IRAC 5.8 and 8.0 μm and MIPS 24 μm detectors, IRAC's two shorter wavelength detectors primarily measured reflected sunlight at 3.6 and 4.5 μm.

Meadows et al. (2004) have looked at the prevalence of asteroids away from the ecliptic plane in the First Look Survey-Ecliptic Plane Component (FLS-EPC). The FLS-EPC is nearly twice as deep as the previous ISO mid-infrared survey (Tedesco & Desert 2002), and has detected a total of 34 asteroids at $\beta = 0^\circ$ and $+5^\circ$, with roughly comparable numbers detected at each latitude. The presence of asteroids away from the ecliptic plane has been noted in a number of *Spitzer* astrophysical studies, including SCOSMOS (Sanders et al. 2007) and SWIRE (Lonsdale et al. 2003; Ryan & Woodward 2009), taken at $\beta = -9^\circ$ and $+17^\circ$, respectively. While the FLS-EPC is the only study of individual solar system small bodies from 3.6 to 24.0 μm, other *Spitzer* studies have characterized near-Earth objects (NEOs) from 3.6 to 8 μm (Mueller et al. 2007; Trilling et al. 2008), MBAs from 3.6 to 8 μm (Ryan & Woodward 2009), the Trojans at 24 μm (Fernandez et al. 2009), and TNOs at 24 μm (Stansberry et al. 2008).

In order to optimize the astrophysical source identification process in mid-infrared data sets, observers may opt to reimage a field so that moving, foreground sources can be clearly distinguished from background objects. This may not be feasible for every observing program, however, and when data are taken over a short period of time, asteroid motion may be less evident. In such cases, it may be a challenge to distinguish between nearby solar system objects, which we will refer to as "local sources," and background objects, which we will refer to as "extrasolar sources" in this paper. To that end, it is of value to compare the mid-infrared spectral energy distributions of local and extrasolar objects, and the FLS-EPC provides the only set of asteroid observations from 3.6 to 24.0 μm.

In this paper, we build upon the Meadows et al. (2004) results and provide detailed photometry from 3.6 to 24 microns for all 34 asteroids detected in the survey. In Section 2, we provide an overview of four *Spitzer* Legacy programs, FLS-EPC, SCOSMOS, SWIRE, and GOODS. In Section 3, we discuss data analysis methods for the FLS-EPC data set, and in Section 4 we provide photometric results at all wavelengths where each asteroid is detected. In Section 5, we examine the mid- and far-IR color of FLS-EPC asteroids in the context of SCOSMOS, SWIRE, and GOODS astrophysical sources and the application of this technique to future mid-infrared and far-infrared observations, including those to be taken during the Warm *Spitzer* Mission, by the *Herschel Observatory*, and by the *WISE* Mission. Finally, in Section 6, we look at the uncertainty in the asteroid colors presented in this paper.

2. OBSERVATIONS

The NASA *Spitzer Space Telescope* was launched into an Earth-trailing orbit on 2003 August 25. The three instruments on board are capable of providing images and spectra from 3.6 to 160 μm to sensitivities as low as a few μJy (Werner et al. 2004). At the start of science operations in 2004 January, the *Spitzer* FLS-EPC was carried out to determine sky plane density of MBAs with diameters as small as $\sim$1 km in the mid-IR.

Thermal constraints require the observatory to look at targets with solar elongations in the range $\epsilon = 80^\circ$–120°. This limitation in observational phase angle, as well as issues of asteroid rate of motion and visibility for a companion ground-based campaign, necessitated careful design of the FLS-EPC program.

2.1. FLS-EPC

The FLS-EPC observed two strips of size 0.13 deg^2 in and near the ecliptic plane, at a solar elongation $\epsilon = 115^\circ$ and ecliptic coordinates (λ,β) = (180.°92, 0.°00) and (180.°92, +5.°00). These fields were observed with IRAC (Fazio et al. 2004) three times in bandpasses centered at 3.6, 4.5, 5.8, and 8.0 μm. Longer wavelength measurements, near the Wien peak for MBAs, were also taken at 24 μm using the Multiband Imaging Photometer for *Spitzer* (MIPS; Rieke et al. 2004), to determine color. At 24 μm an adjacent location to both the $\beta = 0^\circ$ and $+5^\circ$ fields was also observed in the prograde direction, to track any objects that may have moved out of the original field. Finally, a 6° fast scan was taken at this longer wavelength to monitor the zodiacal background. The *Spitzer* FLS-EPC data are publicly available through the archive *leopard* interface http://ssc.spitzer.caltech.edu/propkit/spot/ by querying for program ID 98.

Although the long scan data were taken to look at extended emission rather than point sources, several asteroids seen in the IRAC and MIPS photometry data were also detected in the long scan. IRAC asteroids were identified in MIPS data by extrapolating the 8 μm trail to the 24 μm observations. At 24 μm, asteroids stand out very brightly in comparison to other sources, making their identification more reliable. Data in each of the IRAC three epochs were taken 70 minutes apart, first in the ecliptic plane and then at a latitude of $+5^\circ$. Data for the first MIPS epoch were taken at $\beta = 0^\circ$ immediately following instrument changeover, roughly 5 hr after the last IRAC observations. Table 1 summarizes this program's observing strategy. As shown in Tables 2 and 3, although the majority of sources indicate little

Table 1
FLS-EPC Observation Summary

Instrument (mode)[a]	Epoch	Coordinates (ecliptic, deg)	AOR	Obs Time[b] (hh:mm)
IRAC (map)	1	(180.9175, 0.0000)	6095104	02:35
IRAC (map)	2	(180.9175, 0.0000)	6095360	03:40
IRAC (map)	3	(180.9175, 0.0000)	6095616	04:44
IRAC (map)	1	(180.9175, +5.0000)	6095872	05:50
IRAC (map)	2	(180.9175, +5.0000)	6096128	06:55
IRAC (map)	3	(180.9175, +5.0000)	6096384	07:59
MIPS (slow scan)	4	(180.9175, 0.0000)	6096640	12:42
MIPS (slow scan)	5	(181.0378, 0.0224)	6096896	14:57
MIPS (slow scan)	4	(180.9175, +5.0000)	6097152	16:06
MIPS (slow scan)	5	(181.0378, +5.0224)	6097408	18:33
MIPS (fast scan)	6° scan	(180.9175, +2.9999)	6097664	20:34

Notes.
[a] IRAC and MIPS data were taken at [3.6, 4.5, 5.8, and 8.0] and 24 μm, respectively.
[b] Observations were taken on 2004 January 21 UT.

change on a timescale of 210 minutes, a few objects such as 79364 (1997 EU_4), 99307 (2001 SB_{182}), 5g, and 5i do show light curve variability by a factor of approximately 3–8 in thermal emission at 8 μm.

2.2. *SCOSMOS, SWIRE, and GOODS*

The SCOSMOS fluxes presented in this paper are based on *Spitzer* Cycle 2 observations. SCOSMOS is a highly sensitive survey, with mid-infrared observations down to the micro-Jansky level. The IRAC catalog is derived from the main COSMOS 2 deg^2 "main" field, and the MIPS 24 μm catalog is extracted from the MIPS "deep test area," both at ecliptic latitude $\beta = -9°$, as described by Sanders et al. (2007). The longer wavelength MIPS 70 and 160 μm catalogs are also extracted from the main field, as described by Frayer et al. (2009). Both instruments' source lists have been linked to common background sources and are publicly available through the NASA/IPAC Infrared Science Archive (IRSA).[15] The IRAC catalog correction for total flux, for the 1.″9 aperture, has been derived using coefficients provided by documentation within the SCOSMOS IRSA repository. We have selected objects that are not saturated or contaminated, as designated by "flag = 0" in the catalogs.

The SWIRE data used here correspond to this program's observations nearest the ecliptic plane, the XMM-Newton field at $\beta = +17°$. In considering asteroid colors for other missions such as *WISE*, the GOODS North and South survey (Dickinson et al. 2004; H. Teplitz et al. 2010, in preparation) has readily available flux catalogs at the relevant mid-IR wavelengths (4.5, 8, 12, and 24 μm). Although these fields lie far from the plane at ecliptic latitudes $\beta = +57°$ (GOODS North) and $\beta = -45°$ (GOODS South), where MBAs are less likely to be present, background stellar, galactic, and extragalactic sources exhibit similar SEDs regardless of ecliptic latitudes. Using background GOODS sources rather than SCOSMOS or SWIRE is therefore acceptable.

Spitzer SCOSMOS (program ID 20070), SWIRE (program ID 181), and GOODS (program IDs 3661 and 20599) data are publicly available through *leopard*, through IRSA, or via the Spitzer Heritage Archive http://sha.ipac.caltech.edu/applications/Spitzer/SHA/.

[15] http://irsa.ipac.caltech.edu/

3. FLS-EPC DATA ANALYSIS

Initial asteroid identification (Meadows et al. 2004) in the IRAC and MIPS fields was carried out using the tricolor, or "RGB," technique, wherein each of the three epochs of observation is assigned a color plane in an image display program. These three epochs were then codisplayed using a fixed stellar world coordinate system, which resulted in fixed objects appearing white, while moving targets were seen as red–green–blue quasi-linear sequences of sources. Not all IRAC 8 μm asteroids were linked to MIPS 24 μm observations at the time of Meadows et al. (2004). Since then, we have clearly linked all 8 μm asteroid detections to their counterparts at 24 μm. In Tables 2 and 3, we also include linkages to known objects, provided by Granvik et al. (2007). These updated linkages between FLS-EPC sources and known asteroids are primarily based upon ground-based data taken from 2004 January to March in support of the FLS-EPC and reported to the Minor Planet Center. Orbits are now available for all FLS-EPC numbered or provisionally designated asteroids through the JPL/Horizons database.

The individual epochs and related Astronomical Observation Request (AOR) numbers are provided in Table 1. Raw, unprocessed individual frames as well as software pipeline-generated products are available. The pipeline provides background-subtracted, flat-fielded, and flux-calibrated frames. For the IRAC data, we have worked with the Basic Calibrated Data (BCD) frames rather than mosaics. Given IRAC's pixel scale of 1.″22 pixel^{-1}, the exposure time per frame (30 s), and the average apparent rate of motion of MBAs (10″–20″ hr^{-1}), we have found that asteroid flux in mosaics can be underestimated if the object has moved out of a pixel between successive dithers.

Once the relevant IRAC BCDs for each asteroid have been identified, we have median combined the set of frames to remove cosmic rays and performed aperture photometry in IDL using a 10 pixel aperture radius and sky annulus from pixels [10:20]. Since this is the standard aperture size to which IRAC data are calibrated, aperture correction is not required. As the IRAC observations were well dithered, combining BCDs provides a robust signature for each asteroid, with good signal-to-noise ratio (S/N) and exposure time/pixel ranging from 60 s (at edges) to 420 s, with a majority of sources being observed 240 s pixel^{-1}.

In the case of MIPS, where pixels are four times larger and exposure time between frames, or BCDs, is 10 s, the mosaicing software is effective in retaining stationary sources; MIPS mosaics of the entire field have been used to derive photometry. Background removal by the MIPS pipeline, however, has been found to be inconsistent at the borders of scan legs, and we have generated our own mosaics using the *Spitzer* post-BCD tools MOPEX and APEX[16] to combine the data and derive point-spread function (PSF) photometry.

In general, over the linear range (sources fainter than 500 mJy) of the MIPS 24 μm array, PSF fitting and aperture photometry return very similar values. As a check, we have also run aperture photometry on the MIPS observations and found both methods to be consistent to within 5%. The PSF used in the analysis was obtained from approximately 50 well-behaved sources from the Orion region. The MIPS data were taken as slow spatial scans in the longitudinal direction. These data also provide good S/N, with exposure time/pixel = 100 s for all but the edge positions.

Because flux calibration in the FLS-EPC bands is stellar-based, color correction is applied assuming MBAs are at the

[16] http://ssc.spitzer.caltech.edu/postbcd/mopex.html

Table 2
FLS-EPC $\beta = 0^\circ$ Field

λ (μm)	Epoch	R.A. (deg)	Decl. (deg)	Flux (mJy)	Fluxer (mJy)	Comments
7987 (1981 EV_{22}) [$H = 13.7$][a]						
4.5	[2]	180.627	−0.799	0.0607	0.0266	4.5 μm [2],ll[3] noisy background; 8 μm [1], [3] not centroided due to background source
4.5	[3]	180.626	−0.798	0.0360	0.0222	
8.0	[2]	180.627	−0.799	1.2853	0.1417	
24.0	[4]	180.635	−0.794	13.7900	0.0600	
9981 (1995 BS_3) [$H = 13.5$]						
4.5	[1]	180.747	−0.772	0.1910	0.0456	[3] at edge of FOV
4.5	[2]	180.749	−0.772	0.1624	0.0429	
4.5	[3]	180.753	−0.772	0.3409	0.0606	
8.0	[1]	180.747	−0.772	6.4805	0.2684	
8.0	[2]	180.749	−0.772	7.0203	0.2873	
8.0	[3]	180.753	−0.773	7.6413	0.3043	
24.0	[5]	180.780	−0.776	51.0100	0.7200	
27168 (1991 AN_{21}) [$H = 14.1$]						
4.5	[1]	180.581	−0.808	0.0319	0.0224	4.5 μm, noisy background
8.0	[2]	180.580	−0.81	1.1694	0.1664	
24.0	[4]	180.603	−0.806	14.8600	0.0644	
27293 (2000 AX_{136}) [$H = 13.1$]						
3.6	[1]	180.925	−0.181	0.0763	0.0274	24 μm adjacent scan double, aper phot value used due to ineffective deblending w/PRF photometry
3.6	[2]	180.928	−0.188	0.1309	0.0356	
3.6	[3]	180.931	−0.188	0.1999	0.0439	
4.5	[1]	180.925	−0.181	0.1453	0.0388	
4.5	[2]	180.928	−0.185	0.2446	0.0501	
4.5	[3]	180.931	−0.188	0.3414	0.0589	
5.8	[1]	180.925	−0.181	1.3822	0.1262	
5.8	[2]	180.928	−0.185	1.7605	0.1398	
5.8	[3]	180.931	−0.188	1.8735	0.1415	
8.0	[1]	180.925	−0.181	8.1055	0.2915	
8.0	[2]	180.928	−0.185	11.4411	0.3479	
8.0	[3]	180.931	−0.188	10.4631	0.3314	
24.0	[4]	180.955	−0.210	32.1700	3.5800	
53723 (1999 FZ_{24}) [$H = 13.8$]						
3.6	[2]	180.755	−0.521	0.0982	0.0310	3.6, 4.5 μm [1] underlying source; 4.5 μm [2] noisy background; 24 μm adjacent scan "double," deblending required
3.6	[3]	180.757	−0.520	0.1425	0.0373	
4.5	[2]	180.755	−0.521	0.0494	0.0249	
4.5	[3]	180.757	−0.520	0.1312	0.0378	
5.8	[1]	180.752	−0.522	0.5494	0.0850	
5.8	[2]	180.755	−0.521	0.3707	0.0791	
5.8	[3]	180.757	−0.520	0.3154	0.0745	
8.0	[1]	180.752	−0.522	2.7698	0.1839	
8.0	[2]	180.755	−0.521	2.3037	0.1704	
8.0	[3]	180.757	−0.520	2.2783	0.1736	
24.0	[4]	180.778	−0.508	15.6500	0.0600	
79364 (1997 EU_4) [$H = 16.8$]						
4.5	[1]	180.65	−0.761	0.1032	0.0335	Background sources [2], [3]; 4.5 μm [2] noisy background; 24 μm adjacent scan "double," deblending required Meadows et al. 2004 reported erroneous ID of two separate sources.
4.5	[2]	180.656	−0.762	0.0395	0.0395	
8.0	[1]	180.650	−0.761	0.6527	0.0983	
8.0	[2]	180.656	−0.762	0.5575	0.0991	
8.0	[3]	180.662	−0.763	0.2701	0.0780	
24.0	[4]	180.711	−0.772	1.98	0.0800	
83004 (2001 QY_{160}) [$H = 15.0$]						
3.6	[1]	181.009	−0.041	0.0129	0.0121	3.6 μm, [1],[2] and 4.5 μm[3] noisy background 3.6, 4.5, 5.8 μm [2],[3] have underlying source; 24 μm underlying source (Meadows et al. 2004) and adjacent scan "double;" deblending required

Table 2
(Continued)

λ (μm)	Epoch	R.A. (deg)	Decl. (deg)	Flux (mJy)	Fluxer (mJy)	Comments
3.6	[2]	181.011	−0.041	0.0270	0.0168	
3.6	[3]	181.013	−0.040	0.0401	0.0202	
4.5	[3]	181.013	−0.040	0.0425	0.0233	
8.0	[1]	181.009	−0.041	1.0834	0.1371	
8.0	[2]	181.011	−0.041	0.8968	0.1296	
8.0	[3]	181.013	−0.040	1.2059	0.1450	
24.0	[4]	181.030	−0.035	12.5400	0.0800	
99307 (2001 SB_{182}) [$H = 15.6$]						
4.5	[2]	180.838	−0.317	0.0731	0.0281	4.5 μm [3] noisy background
4.5	[3]	180.840	−0.316	0.0211	0.0164	
8.0	[1]	180.836	−0.317	0.1730	0.0782	
8.0	[2]	180.838	−0.317	0.9295	0.1156	
8.0	[3]	180.840	−0.316	0.1218	0.0692	
24.0	[4]	180.857	−0.312	2.6700	0.0800	
136040 (2002 WL_7) [$H = 15.3$]						
3.6	[1]	180.788	−0.524	0.1150	0.0337	3.6 μm [3] noisy background; 24 μm adjacent scan double, deblending required
3.6	[2]	180.792	−0.525	0.0879	0.0296	
3.6	[3]	180.795	−0.526	0.0250	0.0167	
4.5	[1]	180.788	−0.524	0.1269	0.0365	
4.5	[2]	180.792	−0.525	0.0944	0.0319	
4.5	[3]	180.795	−0.526	0.0784	0.0291	
5.8	[1]	180.788	−0.524	0.5898	0.0985	
5.8	[2]	180.792	−0.525	0.5178	0.0961	
5.8	[3]	180.795	−0.526	0.4531	0.0792	
8.0	[1]	180.788	−0.524	3.5455	0.1992	
8.0	[2]	180.792	−0.525	2.7383	0.1785	
8.0	[3]	180.795	−0.526	3.2844	0.1934	
24.0	[4]	180.816	−0.533	24.3500	0.0600	
2001 QD_{49} [$H = 17.5$]						
8.0	[1]	180.718	−0.472	0.1506	0.0786	Bright, nearby sources 3.6, 4.5, 5.8 μm [2], [3]
8.0	[2]	180.720	−0.473	0.2731	0.0848	
8.0	[3]	180.722	−0.474	0.2740	0.0839	
24.0	[4]	180.741	−0.481	1.1800	0.0600	
2001 RP_{137} [$H = 16.6$]						
3.6	[2]	180.718	−0.560	0.0152	0.0136	3.6 and 4.5 μm noisy background and background source [1], [2]; 8.0 μm [3], extended background source
3.6	[3]	180.719	−0.561	0.0509	0.0230	
4.5	[2]	180.718	−0.560	0.0143	0.0145	
4.5	[3]	180.719	−0.561	0.0301	0.0190	
8.0	[1]	180.715	−0.560	0.4041	0.0925	
8.0	[2]	180.718	−0.560	0.3090.	0.0873	
8.0	[3]	180.719	−0.561	0.3770	0.0916	
24.0	[1]	180.738	−0.564	3.1300	0.0800	
2004 BH_{160} [$H = 18.4$]						
8.0	[1]	180.867	−0.37	0.4192	0.0964	Nearby extended source 3.6, 4.5 μm [1], and 8.0 μm [3]
8.0	[2]	180.869	−0.371	0.1915	0.0827	
8.0	[3]	180.872	−0.373	0.0510	0.0800	
2004 BS_{160} [$H = 18.6$]						
8.0	[1]	181.001	−0.182	0.0865	0.0825	[3] at FOV edge; background sources, 5.8 μm [2], [3]
8.0	[2]	181.004	−0.183	0.1477	0.0903	
2004 BV_{159} [$H = 18.5$]						
8.0	[1]	180.699	−0.513	0.2051	0.0826	All 3.6, 5.8 μm, and 4.5 μm [3] background source. 24 μm adjacent scan "double," deblending required. Not linked with ground-based observation (Granvik et al. 2007).
8.0	[2]	180.703	−0.514	0.6515	0.1129	
8.0	[3]	180.706	−0.515	0.5701	0.1086	
24.0	[4]	180.738	−0.523	1.4600	0.0600	
2004 CA_{105} [$H = 14.7$]						
4.5	[1]	180.664	−0.646	0.5090	0.0242	8 μm [3] background source

Table 2
(Continued)

λ (μm)	Epoch	R.A. (deg)	Decl. (deg)	Flux (mJy)	Fluxer (mJy)	Comments
4.5	[2]	180.664	−0.649	0.1692	0.0422	
5.8	[1]	180.664	−0.646	0.1596	0.0783	
5.8	[2]	180.664	−0.649	0.2405	0.0674	
5.8	[3]	180.665	−0.652	0.1787	0.0645	
8.0	[1]	180.664	−0.646	0.4407	0.1013	
8.0	[2]	180.664	−0.649	0.8251	0.1161	
8.0	[3]	180.665	−0.652	1.0369	0.1281	
24.0	[4]	180.668	−0.678	6.2800	0.0600	
2004 EU_{91} [$H = 18.1$]						
8.0	[1]	180.798	−0.651	0.0876	0.0797	3.6, 4.5 μm [1] and [3] background source; 8 μm[1] noisy background
8.0	[2]	180.801	−0.650	0.5403	0.1089	
8.0	[3]	180.804	−0.650	0.1169	0.0968	
0c						
4.5	[3]	180.712	−0.585	0.0299	0.0193	Not linked with ground-based observation (Granvik et al. 2007); 4.5 μm noisy background
5.8	[1]	180.706	−0.576	0.2953	0.0764	
5.8	[3]	180.712	−0.585	0.0791	0.0578	
8.0	[1]	180.706	−0.576	0.1697	0.0767	
8.0	[2]	180.709	−0.580	0.3940	0.0902	
8.0	[3]	180.712	−0.585	0.1515	0.0707	
24.0	[4]	180.727	−0.636	1.9600	0.0700	
0h						
3.6	[1]	181.005	−0.119	0.0580	0.0245	Not linked with ground-based observation (Granvik et al. 2007); 4.5 μm [3] noisy background; 24 μm adjacent scan double, deblending required
3.6	[2]	181.004	−0.125	0.0771	0.0279	
4.5	[1]	181.005	−0.119	0.1105	0.0342	
4.5	[2]	181.004	−0.125	0.0814	0.0299	
4.5	[3]	181.003	−0.131	0.0317	0.0199	
5.8	[1]	181.005	−0.119	0.1214	0.0555	
8.0	[1]	181.005	−0.119	0.7169	0.1084	
8.0	[2]	181.004	−0.125	0.6709	0.1045	
8.0	[3]	181.003	−0.131	0.6685	0.1035	
24.0	[4]	180.999	−0.173	2.1200	0.0300	

Note. [a] Absolute magnitudes obtained from the JPL/Horizons database.

same temperature as the zodiacal background; the data are divided by color correction factors of [1.035, 1.0835, 1.0588, 1.0931] for the four IRAC channels, as specified in the *Spitzer* Observers Manual,[17] Table 5.5. Color correction at 24 μm is performed by dividing by a correction factor of 0.965, as discussed in Stansberry et al. (2007).

4. ASTEROID PHOTOMETRIC RESULTS

The data presented in this study provide the first systematic, five-wavelength, mid-IR survey of faint asteroids down to the sub-mJy level. In this section, we provide total flux measurements for all 34 asteroids, with detection at wavelengths as short as 3.6 μm for several of the brightest objects. For several of the known MBAs, whose absolute magnitudes H are provided in the JPL Horizons database, we adopt the Standard Thermal Model (STM; Lebofsky & Spencer 1989) to derive infrared asteroid diameters using measured 24 μm flux and then utilize these results to determine geometric albedo p_v.

[17] http://ssc.spitzer.caltech.edu/documents/som/

4.1. IRAC and MIPS Asteroid Flux

Table 2 provides the position, absolute magnitude H (for previously known objects), flux, and flux error at all epochs in the $\beta = 0^\circ$ field, for the wavelengths 3.6, 4.5, 5.8, 8.0, and 24 μm. We only report observations with flux uncertainties that are less than the flux measurements themselves. Table 2's epoch designations indicate whether the measurement is based on IRAC observations (epochs 1, 2, 3) or on MIPS slow scans (4, 5). MIPS has consistently detected all IRAC asteroids that remained in the field of view (FOV) when the 24 μm data were taken. In spite of a factor of ∼4 increase in the zodiacal background from 8 to 24 μm (8.7 mJy/sr versus 39.8 mJy/sr) the S/N is appreciably higher at the longer MIPS wavelength because of the nature of MBA SEDs. Not all objects are detected at the shorter wavelengths because of the sharp drop in MBA flux there, as seen in Figure 1; only the brightest objects have sufficient flux to be observed at 3.6 and 4.5 μm.

Although the initial Meadows et al. (2004) work indicated the presence of 19 moving objects in the $\beta = 0^\circ$ field, we have found that one of the objects (designated 0j) was an

Table 3
FLS-EPC $\beta = +5^\circ$ Field

λ (μm)	Epoch	R.A. (deg)	Decl. (deg)	Flux (mJy)	Fluxer (mJy)	Comments
49266 (1998 UW_5) [$H = 15.7$][a]						
4.5	[2]	182.573	3.803	0.1178	0.0381	
4.5	[3]	182.579	3.804	0.0665	0.0300	
8.0	[2]	182.573	3.803	1.2806	0.1687	
8.0	[3]	182.579	3.804	1.1305	0.1621	
24.0	[4]	182.635	3.807	8.9400	0.0600	
113186 (2002 RG_{106}) [$H = 16.1$]						
3.6	[1]	183.016	4.486	0.0437	0.0214	3.6 μm [2] background source; 24.0 μm [5] adjacent scan double
3.6	[2]	183.018	4.487	0.1080	0.0327	
3.6	[3]	183.02	4.487	0.0265	0.0173	
4.5	[1]	183.016	4.486	0.0681	0.0277	
4.5	[2]	183.018	4.487	0.0579	0.0260	
4.5	[3]	183.02	4.487	0.0323	0.0215	
5.8	[2]	183.018	4.487	0.0855	0.0576	
5.8	[3]	183.020	4.487	0.0394	0.0597	
8.0	[1]	183.016	4.486	0.2712	0.1042	
8.0	[2]	183.018	4.487	0.5115	0.1167	
8.0	[3]	183.02	4.487	0.3536	0.1204	
24.0	[4]	183.034	4.489	2.2700	0.0600	
24.0	[5]	183.037	4.492	1.3100	0.0700	
24.0	[5]	183.037	4.491	1.9100	0.0700	
137958 (2000 CX_{18}) [$H = 16.1$]						
4.5	[1]	182.622	3.826	0.2014	0.0458	
4.5	[2]	182.626	3.829	0.1627	0.0414	
4.5	[3]	182.631	3.832	0.1932	0.0448	
8.0	[1]	182.622	3.826	5.6508	0.2471	
8.0	[2]	182.626	3.829	4.3519	0.2181	
8.0	[3]	182.631	3.832	4.3796	0.2187	
24.0	[4]	182.674	3.862	15.8500	0.0600	
140479 (2001 TQ_{138}) [$H = 16.0$]						
4.5	[3]	182.739	3.776	0.0357	0.0223	8.0 μm noisy background
8.0	[1]	182.734	3.773	0.2053	0.0840	
8.0	[2]	182.737	3.775	0.1816	0.0958	
8.0	[3]	182.739	3.776	0.1056	0.1930	
2004 BU_{99} [$H = 17.4$]						
3.6	[1]	182.784	4.287	0.0186	0.0144	5.8 μm [1] inconsistent sampling over background annulus
3.6	[2]	182.79	4.283	0.0191	0.0143	
3.6	[3]	182.795	4.279	0.0640	0.0251	
4.5	[2]	182.790	4.287	0.0413	0.0218	
4.5	[3]	182.795	4.283	0.0317	0.0195	
5.8	[1]	182.784	4.279	0.4607	0.0967	
8.0	[1]	182.784	4.287	0.2152	0.0640	
8.0	[2]	182.79	4.283	0.5062	0.0980	
8.0	[3]	182.795	4.279	0.5667	0.1001	
2004 EE_{58} [$H = 16.0$]						
4.5	[1]	182.607	3.852	0.0135	0.0158	
4.5	[3]	182.611	3.85	0.0359	0.0216	
8.0	[1]	182.607	3.852	0.3273	0.1134	
8.0	[2]	182.609	3.851	0.4653	0.1138	
8.0	[3]	182.611	3.850	0.6815	0.1248	
24.0	[4]	182.625	3.842	4.6500	0.0600	
5b						
3.6	[2]	182.74	3.948	0.0678	0.0259	3.6 μm [1], [3] background source; 24 μm adjacent scan "double"
4.5	[1]	182.736	3.947	0.0805	0.0298	
4.5	[2]	182.74	3.948	0.0663	0.0274	
4.5	[3]	182.743	3.948	0.0409	0.0220	
5.8	[1]	182.736	3.947	0.2155	0.0583	
5.8	[2]	182.74	3.948	0.1304	0.0493	
5.8	[3]	182.743	3.948	0.3152	0.0685	
8.0	[1]	182.736	3.947	0.9839	0.1319	

Table 3
(Continued)

λ (μm)	Epoch	R.A. (deg)	Decl. (deg)	Flux (mJy)	Fluxer (mJy)	Comments
8.0	[3]	182.743	3.948	1.0103	0.1289	
24.0	[4]	182.771	3.955	2.2700	0.0600	
24.0	[4]	182.772	3.955	2.1500	0.0600	
5c						
4.5	[2]	182.732	3.824	0.0158	0.0147	8.0 μm noisy background
4.5	[3]	182.737	3.825	0.0960	0.0320	
8.0	[1]	182.728	3.823	0.2221	0.0781	
8.0	[2]	182.732	3.824	0.1166	0.0681	
8.0	[3]	182.737	3.825	0.1010	0.0702	
5d						
3.6	[1]	182.768	4.082	0.1066	0.0325	
3.6	[3]	182.774	4.084	0.2028	0.0444	
4.5	[1]	182.768	4.082	0.0726	0.0281	
4.5	[2]	182.771	4.083	0.3732	0.0615	
4.5	[3]	182.774	4.084	0.1366	0.0378	
5.8	[1]	182.768	4.082	0.1494	0.0624	
5.8	[2]	182.771	4.083	0.3896	0.0829	
5.8	[3]	182.774	4.084	0.2112	0.0711	
8.0	[1]	182.768	4.082	0.5751	0.0996	
8.0	[2]	182.771	4.083	0.8056	0.1131	
8.0	[3]	182.774	4.084	0.5839	0.1004	
5e						
3.6	[2]	182.775	4.115	0.0710	0.0267	5.8 μm [1] inconsistent sampling over aperture in stacked image; background annulus 8 μm noisy background
3.6	[3]	182.778	4.115	0.0038	0.0086	
4.5	[2]	182.775	4.115	0.1036	0.0329	
4.5	[3]	182.778	4.115	0.0203	0.0161	
5.8	[2]	182.775	4.115	0.0842	0.0552	
8.0	[1]	182.772	4.114	0.2530	0.0875	
8.0	[2]	182.775	4.115	0.2396	0.0793	
8.0	[3]	182.778	4.115	0.1013	0.0684	
5f						
3.6	[1]	182.714	4.016	0.0433	0.0212	
3.6	[2]	182.718	4.015	0.0573	0.0241	
4.5	[1]	182.714	4.016	0.0214	0.0167	
5.8	[1]	182.714	4.016	0.0723	0.0563	
5.8	[2]	182.718	4.015	0.1990	0.0658	
5.8	[3]	182.722	4.013	0.0823	0.0541	
8.0	[1]	182.714	4.016	0.3187	0.0886	
8.0	[2]	182.718	4.015	0.3281	0.0879	
8.0	[3]	182.722	4.013	0.3012	0.0876	
5g						
3.6	[2]	182.82	4.036	0.0192	0.0150	5.8 μm extended background structure under sky annulus; 8.0 μm, all epochs, noisy background
3.6	[3]	182.824	4.037	0.0580	0.0243	
4.5	[1]	182.816	4.035	0.0279	0.0184	
4.5	[3]	182.824	4.037	0.0088	0.0127	
5.8	[1]	182.816	4.035	0.0647	0.0613	
5.8	[2]	182.82	4.036	0.3237	0.0903	
5.8	[3]	182.824	4.037	0.1503	0.0661	
8.0	[1]	182.816	4.035	0.1230	0.0696	
8.0	[2]	182.82	4.036	0.0896	0.0712	
8.0	[3]	182.824	4.037	0.2314	0.0864	
5i						
4.5	[2]	182.855	4.458	0.0577	0.0251	3.6 μm background source; 4.5 μm [1], [3] background source
5.8	[2]	182.855	4.458	0.1608	0.0660	
5.8	[3]	182.862	4.458	0.0999	0.0569	
8.0	[1]	182.849	4.459	0.2622	0.0845	
8.0	[2]	182.855	4.458	0.3730	0.0873	
8.0	[3]	182.862	4.458	0.2419	0.0780	

Table 3
(Continued)

λ (μm)	Epoch	R.A. (deg)	Decl. (deg)	Flux (mJy)	Fluxer (mJy)	Comments
5j						
3.6	[3]	182.893	4.429	0.0340	0.0190	5.8 μm [3] and 8.0 μm [3] noisy background
4.5	[2]	182.891	4.428	0.2141	0.0469	
5.8	[1]	182.887	4.428	0.3795	0.0747	
5.8	[2]	182.891	4.428	0.2731	0.0658	
5.8	[3]	182.893	4.429	0.0331	0.0478	
8.0	[1]	182.887	4.428	0.3544	0.0862	
8.0	[2]	182.891	4.428	0.2840	0.0811	
8.0	[3]	182.893	4.429	0.1124	0.0687	
5k						
3.6	[2]	182.916	4.469	0.0613	0.0249	
4.5	[1]	182.913	4.468	0.4494	0.0674	
4.5	[2]	182.916	4.469	0.0595	0.0255	
4.5	[3]	182.919	4.47	0.0736	0.0282	
5.8	[1]	182.913	4.468	0.4339	0.0812	
8.0	[1]	182.913	4.468	1.0597	0.1225	
8.0	[2]	182.916	4.469	0.8622	0.1142	
8.0	[3]	182.919	4.470	1.0134	0.1190	
5l						
3.6	[1]	182.914	4.328	0.0209	0.0151	3.6, 4.5 μm [2] background source; 5.8, 8.0 μm [1] extended background source
3.6	[3]	182.936	4.326	0.0598	0.0244	
4.5	[1]	182.914	4.328	0.0037	0.0097	
5.8	[2]	182.924	4.327	0.2302	0.0713	
8.0	[2]	182.924	4.327	0.2266	0.0762	
8.0	[3]	182.936	4.326	0.2243	0.0785	

Note. [a] Absolute magnitudes obtained from the JPL/Horizons database.

Table 4
FLS-EPC MIPS 24 μm Long Scan Strip, $\beta = 0^\circ$ to $+6^\circ$

Asteroid[a]	R.A. (deg)	Decl. (deg)	Flux (mJy)	Fluxer (mJy)
0h	180.992	−0.217	5.60	0.071
27293 (2000 AX_{136})	180.975	−0.229	65.19	0.06
136040 (2002 WL_7)	180.837	−0.542	35.28	0.06
140479 (2001 QY_{160})	181.044	−0.029	19.07	0.06

Note. [a] All sources were also identified at $\beta = 0^\circ$ in IRAC observations.

artifact of the pipeline mosaicing software. Nine of these objects are well characterized and numbered. Seven have provisional designations, and five of these designations are based on the ground-based observations described by Granvik et al. (2007). Only two of the objects are currently not linked with ground-based data, and these are labeled with a "0" in Table 2 to indicate their latitude and a letter that indicates the order in which they were identified in the initial analysis phase of this work in 2004. The flux values provided in Table 2, as well as those values provided in Tables 3 and 4 (discussed below), provide photometry in and above the ecliptic plane for mid-IR observations at 3.6, 4.5, 5.8, 8.0, and 24 μm; these results extend the work of Meadows et al. (2004) which only provided photometry at the two longest wavelengths for known asteroids and did not include the scan strip. The FLS-EPC is a highly sensitive survey and, at the time the data were taken, the survey increased the number of known asteroids in the $\beta = 0^\circ$ field by nearly a factor of 2 (Meadows et al. 2004; Tedesco et al. 2005; Ryan & Woodward 2009).

Table 3 provides photometric results for the $\beta = +5^\circ$ field, where 16 sources have been observed. The columns for this table are identical to those in Table 2. Four of the objects identified at this latitude are numbered, and two have provisional designations. The remaining 10 are newly identified by the FLS-EPC and are designated with the number "5" for their ecliptic latitude and a letter, in a similar fashion to objects found in the ecliptic plane. As these objects are less bright, only two have been identified at 3.6 μm. This higher latitude population is 30% fainter than the ecliptic asteroids. A mean 8 μm flux at each latitude, averaged for rotation, is F8($\beta = 5^\circ$) = 0.730 mJy, while F8($\beta = 0^\circ$) = 1.253 mJy. The FLS-EPC is a small sample, but this observed brightness drop may be suggestive of a smaller population of asteroids with distance above the ecliptic plane.

Finally, we provide flux measurements for four objects that were also identified in the 6° scan in Table 4. These observations were taken at the end of the FLS-EPC survey, as shown in Table 1.

The brightest objects detected in the ecliptic plane are 9981 and 27293. Their fluxes at 8 and 24 μm provide colors $F(24/8)$ ∼7 and 3, respectively, using a time-averaged value for $F(8\ \mu\text{m})$. The brightest objects detected above the ecliptic plane are 49266 and 137958, with $F(24/8)$ ∼7 and 3, respectively. In Meadows et al. (2004), an average color $F(24/8)$ ∼10 was reported, and we believe this was due to reliance on only one epoch for the 8 μm measurements, rather than a rotational average. Additionally, the 8 μm photometry was done on the large mosaiced image and, as detailed in Section 3, more accurate values are derived using individual BCDs. Asteroid colors are further discussed in Section 5 below, and uncertainty in color is discussed in Section 6.

4.2. Thermal Modeling

Approaches to thermal modeling of solar system objects are handled in a variety of ways, from the basic STM (Lebofsky et al. 1986), which assumes objects are non-rotating spheres, to the more detailed near-Earth thermal model (NEATM; Harris 1998), which considers observations at non-opposition. Both of these models, unlike the Fast Rotator Model (FRM; Lebofsky & Spencer 1989), assume thermal emission occurs only on the sunward side and that asteroids do not lose thermal emission on the nightside. Additional observational parameters such as an asteroid's spin axis, shape, thermal inertia, surface roughness, and emissivity are considered in the thermophysical model (Mueller 2002). While the focus of this paper is color differentiation of solar system objects from background observations, in this section we use the STM to estimate diameters for the previously known FLS-EPC asteroids. MBAs are less susceptible to the YORP effect (Bottke et al. 2006; Wolters et al. 2008). They are expected to have slower spin rates and more mature surfaces with regolith. The presence of regolith rather than bare rock suggests a lower thermal inertia, thereby decreasing thermal emission on the nightside. Rather than using the FRM, it is possible to use the STM or NEATM (Wolters et al. 2008; Fernandez et al. 2009), and we consider the STM in this section, since shape and spin axis are not known for our objects. To compare our measurements to the STM, we employ the value for the absolute magnitude H provided by JPL/Horizons. Absolute magnitude is defined for a solar system object as the visual magnitude it would have at 1 AU from the Sun, 1 AU from the observer, at astronomical opposition (Sun–target–observer angle = 0°). While this is an unphysical quantity, it serves as a useful measure of the relative brightness of objects within our solar system. We must also consider the role of albedo, the fraction of incident light which is reflected by the object, when comparing observed fluxes to the model. MBAs exhibit a bimodal albedo distribution, with darker, carboneous "C-type" asteroids having typical albedo values $p_v \sim 0.05$ and brighter, stony, silicate-based "S-type" asteroids with $p_v \sim 0.20$ (dePater & Lissauer 2001, p. 353).

Infrared diameter for FLS-EPC asteroids is calculated using the MIPS flux at 24 μm, where emission is purely thermal for MBAs. We assume an initial value for the geometric albedo, p_v, in the relation

$$F_{\rm infrared}(\lambda) = \frac{\epsilon d_{\rm ast}^2}{2\Delta^2} \int_0^{\pi/2} B(\lambda, T_{ss}(\theta)) \sin(\theta)\cos(\theta) d\theta,$$

where $d_{\rm ast}$ is the asteroid diameter, Δ is the distance from the observer, ϵ is the emissivity, and B(λ,T_{ss}) is the Planck function at the observed wavelength and temperature. In the STM (Lebofsky & Spencer 1989), the temperature distribution $T_{\rm ss}$ for a non-rotating body is

$$T_{\rm ss} = \left[\frac{S_\odot}{\epsilon\sigma\eta r^2}(1 - q p_v)\right]^{\frac{1}{4}},$$

where $S_\odot$ is the solar constant, σ is the Stefan–Boltzmann constant, r is distance from the Sun. We adopt values of emissivity $\epsilon = 0.9$ and beaming parameter, $\eta = 0.756$. The albedo p_v is attenuated by the phase integral q, as the STM assumes data are taken at opposition. The phase integral integrated over all phase angles (Bowell et al. 1989) yields $q = 0.290 + 0.684G$, where $G = 0.15$ is the slope parameter, a measure of the gradient of the phase curve. We assume an initial $p_v = 0.20$; the infrared flux, and by association the infrared diameter, is relatively insensitive to the albedo, and varies by <2% in the range $0.05 < p_v < 0.20$. For asteroid 7987, for example, $p_v = 0.05$ yields $d_{\rm ast} = 4.006$ km and $p_v = 0.20$ results in $d_{\rm ast} = 4.097$ km.

Once the infrared diameter is determined using 24 μm flux measurements, we can use the absolute magnitude H to constrain the geometric albedo p_v using the relation (Tedesco et al. 1992, p. 17)

$$d_{\rm ast} = \frac{1329}{\sqrt{p_v}} 10^{-0.2H}.$$

Table 5 provides the JPL/Horizons absolute magnitude H for all 16 known asteroids in the FLS-EPC. Using purely thermal, observed 24 μm flux (Tables 2 and 3), H, and assuming $p_v = 0.20$, since the majority of asteroids are S-type, we derive the STM infrared diameter $diam$ for all known asteroids in the FLS-EPC. In Table 5 $diam$ is used to obtain an infrared, geometric albedo p_v, as described in the equation above. We also present modified magnitude, albedo, and diameter, H', p_v', and $diam'$, as discussed below.

Since the majority of MBAs are known to be carbonaceous C-type ($p_v \sim 0.04$–0.06) or stony S-type ($p_v \sim 0.14$–0.17; dePater & Lissauer 2001, p. 353), we expect our sample to provide a similar range of albedos. We find, however, that over half of our objects have $p_v \geqslant 0.25$, values typically associated with less prevalent, bright MBAs of the E-type, which have albedos in the range 0.25–0.6.

As it is improbable that a significant portion of our population is of the rare E-type, the albedos presented in Table 5 are likely too high. We can improve results from the STM by applying empirically derived adjustments to H (Juric et al. 2002; Romanishin & Tegler 2005; Parker et al. 2008) and p_v (Granvik et al. 2007; Parker et al. 2008; Ryan & Woodward 2009). Comparisons of observed and predicted magnitudes in the Sloan Digital Sky Survey (Juric et al. 2002; Parker et al. 2008) report an average offset of $H' \sim H + 0.4$, which we provide in Table 5. The taxonomic types for these objects are not known. We assign a first-order classification of either C-type or S-type based on recent work by Ryan & Woodward (2009), who report type-based segregation of MBAs with distance from the Sun, with objects in the inner main belt more likely to be S-type, while outer main belt objects are typically likely to be C-type. Using the FLS-EPC asteroid distances reported by Granvik et al. (2007) and assuming C-type $p_v \sim 0.05$ and S-type $p_v \sim 0.20$, we derive revised diameters $diam'$ (Tedesco et al. 1992, p. 17). For 14 of the 16 objects, using observational corrections to H and distance-based corrections to determine albedo, we find that $diam'(H', p_v')$ is within a factor of 2 of $diam(H, p_v)$. For the remaining two asteroids, corrected diameters vary by a factor of approximately 2.5. These variations may be due to rotational variability (Harris et al. 2009) or incorrect taxonomic type. While the primary purpose of this paper is to look at asteroid color, here we demonstrate that, even with observed thermal fluxes, use of the STM and Horizons magnitudes provides unphysical geometric albedos. Applying more sophisticated models such as NEATM or the thermophysical model is beyond the scope of this paper, but additional observations to determine rotational period, spin axis, and taxonomic type may provide further information on diameter, albedo, and surface roughness of the FLS-EPC asteroids. Asteroid color in comparison to background sources is discussed in detail in Section 5 below.

Table 5
FLS-EPC Standard Thermal Model Infrared Diameters for Previously Known Asteroids

Asteroid	EcLat (deg)	Distance (AU)	H	p_v	*Diam* (km)	H'	p'_v	*Diam*' (km)[a]
7987 (1981 EV_{22})	0	3.10	14.000	0.347	4.103	14.400	0.05[b]	4.098
9981 (1995 BS_3)	0	2.65	13.500	0.208	5.814	13.900	0.05[b]	5.827
27168 (1999 AN_{21})	0	n/a	14.100	0.324	3.534	14.500	0.20[d]	3.741
27293 (2000 AX_{136})	0	2.40	13.100	0.703	3.802	13.500	0.20[c]	5.929
53273 (1999 FZ_{24})	0	3.10	13.800	0.283	4.344	14.200	0.05[b]	0.649
79364 (1997 EU_4)	0	2.00	16.800	0.806	0.646	17.200	0.20[c]	1.079
83004 (2001 QY_{160})	0	2.96	15.000	0.139	3.570	15.400	0.05[b]	3.546
99307 (2001 SB_{182})	0	3.02	15.300	0.457	1.713	15.700	0.05[b]	3.821
136040 (2002 WL_7)	0	2.69	15.300	0.078	4.143	15.700	0.05[b]	1.717
2001 QD_{49}	0	2.77	17.500	0.191	0.961	17.900	0.05[b]	1.780
2001 RP_{137}	0	2.93	16.600	0.132	1.749	17.000	0.05[b]	4.156
2004 CA_{105}	0	2.80	14.700	0.456	2.260	15.100	0.05[b]	2.362
49266 (1998 UW_5)	5	2.22	15.700	0.315	1.716	16.100	0.20[c]	1.791
113186 (2002 RG_{106})	5	2.69	16.100	0.204	1.773	16.500	0.05[b]	2.267
137958 (2000 CX_{18})	5	2.26	16.100	0.116	2.354	16.500	0.15[c]	1.489
2004 EE_{58}	5	2.98	16.000	0.145	2.202	16.400	0.05[b]	0.965

Notes.
[a] Diameters derived using H' and p'_v.
[b] Type-C.
[c] Type-S.
[d] Distance not available, assume Type-S.

5. MID-INFRARED COLOR OF SOLAR SYSTEM AND BACKGROUND SOURCES

MBAs are routinely evident in *Spitzer* science programs intended to target stationary, background objects. Observers may opt to reimage a field to identify transients, which are not evident at the same location in the sky in time-separated exposures. However, using relative motion to flag foreground sources may not be feasible in cases where repeated observations are not available. While MBAs are a source of uncertainty in IRAC and MIPS 24 μm data, trans-Neptunian objects (TNOs), which lie farther out in the solar system and are subsequently colder, exhibit a Wien peak at 40–60 μm, making them a possible source of "foreground contamination" for missions such as the *Herschel Space Observatory* (Pilbratt et al. 2010), which operates in the wavelength range 55–670 μm. The time separation required to reimage a field and identify TNOs in *Herschel* is substantially longer for *Herschel* than it is for *Spitzer*, since TNOs move at an appreciably slower rate than MBAs (1″–2″ hr^{-1} for TNOs versus 10″–30″ hr^{-1} for MBAs). In addition, a larger pixel size for *Herschel* PACS instrument (6″–10″ pixel^{-1}) requires a more substantial temporal separation between exposures to discern *Herschel* TNOs from extrasolar sources as compared to *Spitzer* (1.″22 and 2.″54 pixel^{-1} for IRAC and MIPS).

Because space-based observing time is limited and users may wish to avoid duplicating observations if possible, we present a technique that may be used in some cases for foreground source differentiation, when the exploitation of relative motion of foreground objects is not possible.

In Section 5.1, we examine the FLS-EPC asteroid color in the context of two *Spitzer* Legacy data sets, SCOSMOS (Sanders et al. 2007) and SWIRE (Lonsdale et al. 2003), taken near the ecliptic plane at 3.6 to 24.0 μm. In Section 5.2, we look at color–color differentiation between NEOs, MBAs, TNOs, and background astrophysical sources that may be observed during the *Spitzer* warm mission, where only the 3.6 and 4.5 μm IRAC channels are used due to cryogen depletion. In Section 5.3, we look at the MBA color at mid- and far-infrared wavelengths, as may be observed by the *Herschel* mission, in comparison to astrophysical objects. Multiband, mid-infrared, simultaneous asteroid data are being taken by the *WISE* spacecraft, and the identification of moving solar system objects in *WISE* data, in the context of GOODS observations, is discussed in Section 5.4.

5.1. Spitzer Cryogenic Mission

The FLS-EPC is a unique *Spitzer* program as it was specially designed to minimize the instrument transition time from IRAC to MIPS. Typically, up to 12 hr are required for an instrument change, and MBAs move out of the FOV during the elapsed time, but FLS-EPC IRAC and MIPS observations are separated by less than 5 hr. Although the FLS-EPC observed closer to the ecliptic plane ($\beta = 0°$ and $+5°$) than the SCOSMOS ($\beta = -9°$) and SWIRE *XMM-Newton* programs ($\beta = +17°$), it is reasonable to compare these data sets, since MBAs at all latitudes lie at a comparable distance from the sun and thus are at approximately the same temperature. As a consequence, these MBAs will have similar SEDs.

Lacy et al. (2004) and Stern et al. (2005) have looked at the mid-infrared color of non-stellar astrophysical sources, AGNs in particular, from 3.6 to 24 μm, using the *Spitzer* Extragalactic First Look Survey and the IRAC Shallow Survey, respectively. Lacy et al. (2004) have identified a "box" where X-ray and type-1 AGNs are often seen, and Stern et al. (2005) have confirmed the presence of such a region in color space that can be used to potentially identify AGNs, particularly for shallower data sets.

In a similar fashion to these papers, we provide colors at IRAC and MIPS wavelengths in Figures 2, 3, and 4. We look at asteroids in comparison to the deep SCOSMOS survey ($\beta = -9°$; Figure 2; Figure 3, left panel; and Figure 4, left panel) and the shallower SWIRE survey ($\beta = +17°$ field; right panels of Figures 3 and 4). The IRAC SCOSMOS project "main" area looked at a 2 deg^2 area of sky, and its stationary, background sources are plotted here as dots. The SCOSMOS source list includes thousands of stars, galaxies, and AGNs, which are designated by blue, green, and red dots, respectively. In Figures 3 and 4, FLS-EPC sources are plotted as diamonds, with the

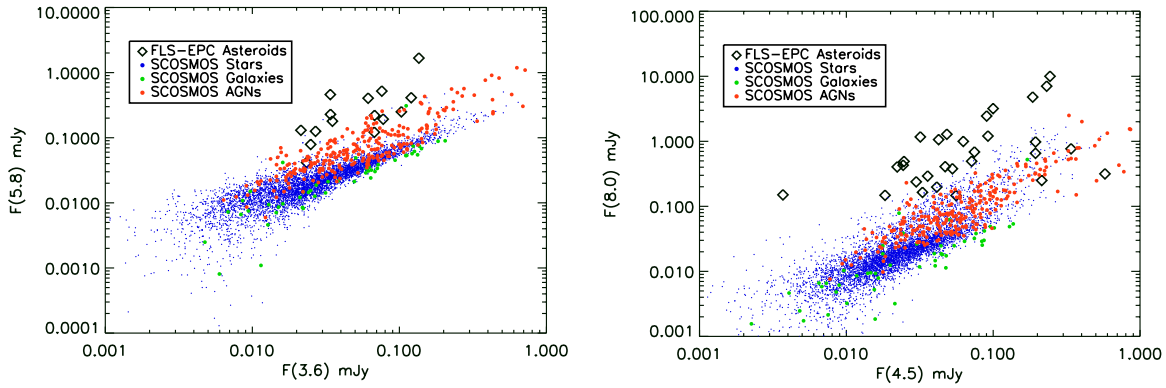

Figure 2. Left: FLS-EPC and SCOSMOS source colors, $F(5.8)$ and $F(3.6)$. Stars (blue dots), galaxies (green dots), and AGNs (red dots) are compared to asteroids (black diamonds). Right: $F(8)$ plotted against $F(4.5)$; symbols are same as the left figure. In color space, asteroids generally exhibit an excess at 5.8 μm and 8 μm, as compared to extrasolar sources. While stars and galaxies are significantly bluer than asteroids, as expected, AGNs are somewhat red and less easily distinguished at these wavelengths.

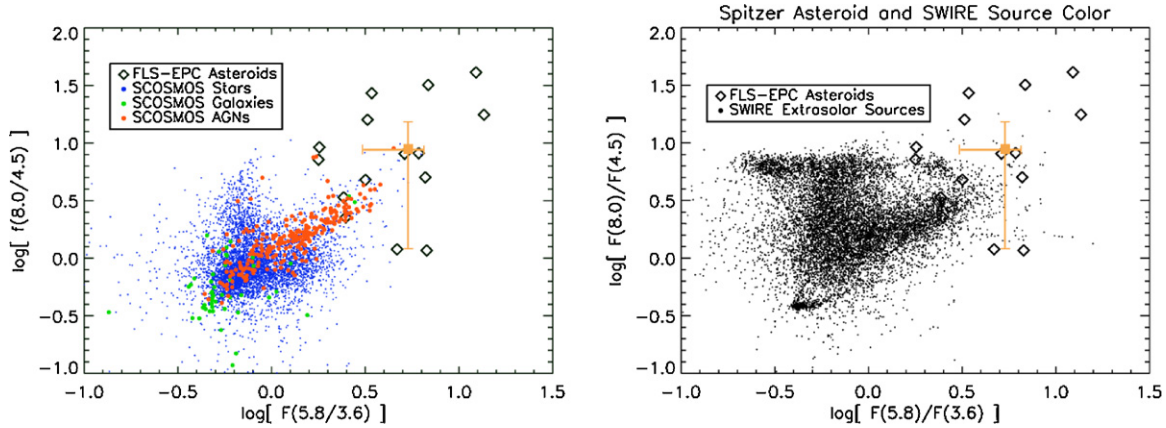

Figure 3. Color–color plots of asteroids, stars, galaxies, and AGNs. Nearly all asteroids are present in a distinct region in color space. The left panel shows SCOSMOS sources, ($\beta = -9°$), plotted as solid dots, and FLS-EPC asteroids plotted as diamonds. Stars (blue dots) and galaxies (green dots) are significantly bluer that asteroids (diamonds), as expected. AGNs (red dots), though redder than stellar and galactic sources, are still bluer than asteroids at these wavelengths. The solid yellow square with error bars indicates median asteroid color and the associated median absolute deviation. At a greater distance from the ecliptic plane, ($\beta = +17°$), we see the same effect in SWIRE *XMM-Newton* (solid dots) when their color is plotted against asteroids (diamonds) in the right panel. The consistent differentiation between local and extrasolar sources at more than one ecliptic latitude may be exploited in future studies, as discussed in Section 5.4.

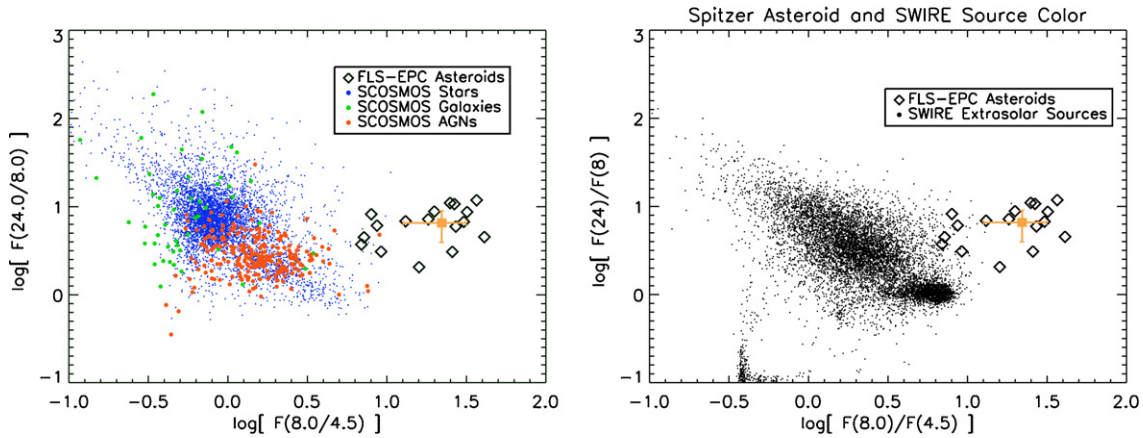

Figure 4. Same as Figure 3, at longer wavelengths. Asteroids are even more distinguishable when MIPS and IRAC colors are considered. These color–color plots are similar to ones that can be generated with *WISE* data. *WISE* asteroids (see the table) will appear down and to the right in comparison to background sources, as discussed in Section 5.4.

median asteroid color designated by an orange square. We do not provide median flux values in Figure 2, as flux is primarily a proxy for size, whereas color is an indicator of mid-infrared thermal emission and independent of the sensitivity of *Spitzer* observations.

Because of flux uncertainty due to the rotational variability of asteroids, we have chosen to compute colors based on IRAC passbands with similar FOVs. As discussed in Section 2.1 and shown in Tables 2 and 3, rotational variability can introduce differences in flux of up to a factor of 8. The 3.6 and 5.8 μm

(referred to as the "shorter wavelength FOV") detectors take images at the same time, as do the 4.5 and 8.0 μm (referred to as the "longer wavelength FOV") detectors.

For the shorter IRAC wavelength FOV, 3.6 and 5.8 μm, SCOSMOS stars and galaxies are generally bluer than the asteroids, as shown in Figure 2, left panel. In the case of AGNs, differentiation using only these two bandpasses is less feasible. For the longer IRAC wavelength FOV, 4.5 and 8.0 μm, Figure 2, right panel, asteroids generally appear to be much redder, with $F(8\,\mu\mathrm{m})/F(4.5\,\mu\mathrm{m}) > 1$ in all instances.

A look at the color–color relation for asteroids and extrasolar sources (Figure 3) reinforces the differentiation seen in Figure 2. For the shorter IRAC wavelength FOV, 3.6 and 5.8 μm, SCOSMOS stars and galaxies are generally bluer than the asteroids, as seen in Figure 3, left panel. In the case of AGNs, differentiation using only these two bandpasses is less feasible. For the longer IRAC wavelength FOV, 4.5 and 8.0 μm, asteroids generally appear to be much redder, with $F(8\,\mu\mathrm{m})/F(4.5\,\mu\mathrm{m}) > 1$ in all cases, as seen in Figure 3.

At 24 μm, near the MBA Wien peak, we consider the deeper MIPS "test area," which looked at a 0.17 deg^2 area of sky, as well as the SWIRE *XMM-Newton* data at this longer wavelength. A unique region in color–color space is clearly apparent in Figure 4, where $F(24/8)$ is plotted against $F(8/4.5)$. MBAs lie in a different region of color space due to their temperatures. For the objects shown in Figure 4, temperatures derived from *Spitzer* colors range from 221 K to 271 K. In Figure 3, two asteroids appear to have anomalously low 5.8/3.6 color. These objects, 0h and 2002 RG106, may have low fluxes at the shorter IRAC wavelengths due to high albedo. For higher albedo sources, thermal emission at shorter wavelengths will be relatively lower and more comparable to the contribution from reflected sunlight. One of these two asteroids, 2002 RG106, has a background source in the 3.6 μm observation that limits measurement accuracy.

We have considered the robustness of this technique by deriving similar color–color plots for astrophysical sources seen farther away from the ecliptic plane. The right panels of Figures 3 and 4 show color–color plots of SWIRE *XMM-Newton* data at the same wavelengths, 3.6 and 5.8 μm, in Figure 3. Again, the presence of the majority of our asteroids in their own region of color space is apparent. The larger number of extrasolar sources seen in the SWIRE *XMM-Newton* data set can be attributed to the larger FOV for this Legacy project ($\sim$9 deg^2 versus $\sim$2 deg^2 for SCOSMOS IRAC and $\sim$0.17 deg^2 for deep SCOSMOS MIPS).

The median colors for the FLS-EPC asteroids are $[F(5.8/3.6), F(8.0/4.5), F(24/8)] = (4.9 \pm 1.8, 8.9 \pm 7.4, 6.4 \pm 2.3)$. The uncertainty in color, the median absolute deviation, is a more robust second moment estimator and defined as $mad = med(|x_i - med(x)|)$ and, assuming a Gaussian distribution, designates a value $\pm 1.4\sigma$ of the median.

In Figures 3 and 4, only asteroids with measurable flux in the relevant wave bands are included, and this affects the median colors in each plot. In Figure 3, the orange box and error bars show a median $[F(5.8/3.6), F(8.0/4.5)] = (4.9 \pm 1.8, 8.1 \pm 6.9)$. Similarly, in Figure 4 a median color is shown: $[F(8.0/4.5), F(24/8)] = (22.4 \pm 8.8, 6.4 \pm 2.3)$. The difference in $F(8/4.5)$ color between the two plots is likely due to small sample size. Missions such as *WISE* are routinely detecting MBAs in four bandpasses, as discussed in Section 5.4, and consequently can provide improved data on asteroid color.

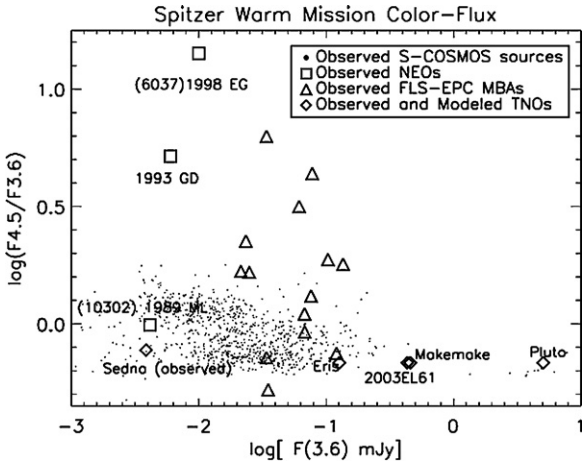

Figure 5. In addition to exploiting the relative motion of NEOs, MBAs, and TNOs to distinguish them from background sources, we may also consider color differences for the majority of these types of objects. Here, we plot measured and modeled NEO, MBA, and TNO color in comparison to SCOSMOS Cycle 2 and 3 sources for IRAC 3.6 and 4.5 μm. We see that, depending on albedo, NEOs and MBAs may be distinguished from background sources based on color. TNOs are appreciably farther from the Sun and can only be detected in reflected sunlight at these wavelengths. Given a time separation of several hours, however, it may be possible to detect TNOs by their relative motion. NEO fluxes are from Mueller et al. (2007) and Trilling et al. (2008), MBA fluxes are from this work, and TNO observed fluxes are from Stansberry et al. (2008).

While *Spitzer* observers are encouraged to take multiple-epoch observations to distinguish between asteroids and background sources, the identification of an "asteroid region" in color space may allow for further differentiation between sources in cases of timespan-limited data or if MBAs happen to be slow movers because of viewing geometry. This technique may be used to distinguish between these and other types of mid-IR sources.

5.2. The Spitzer Warm Mission and NEOs, MBAs, and TNOs

Solar system objects at a variety of distances from the Sun, including NEOs ($\lambda_{\mathrm{Wien}} \sim 8\,\mu$m, rate $\sim$100″–200″ hr^{-1} near opposition), MBAs ($\lambda_{\mathrm{Wien}} \sim 20\,\mu$m, rate $\sim$10″–30″ hr^{-1} near opposition), and TNOs ($\lambda_{\mathrm{Wien}} \sim$ 40–70 μm, rate $\sim$1″–2″ hr^{-1} near opposition) may be detected by the *Spitzer* Warm Mission. Several NEOs have been observed during the *Spitzer* cryogenic mission (Mueller et al. 2007; Trilling et al. 2008), and we examine these sources to compare their colors to extragalactic sources in Figure 5, where we plot the 4.5/3.6 μm color versus 3.6 μm flux for these types of solar system small bodies in comparison to SCOSMOS sources. A color difference is apparent between the majority of MBAs and NEOs and extrasolar sources, depending on the albedo of the solar system source. While a time-separated observing strategy will exploit the relative motion of NEOs and MBAs against background sources as a primary means of identification, we may also exploit their unique color signature for the purpose of detection, for a majority of sources, as shown in Figure 5. In the case of TNOs, where apparent motion is much slower, a time separation of a few hours may be required, as the color difference between these objects and stars is not readily apparent. It should be noted that apparent rates across the sky as viewed by *Spitzer* at quadrature may be appreciably lower than the values presented above, making it potentially more challenging to distinguish between nearby and more distant solar system objects.

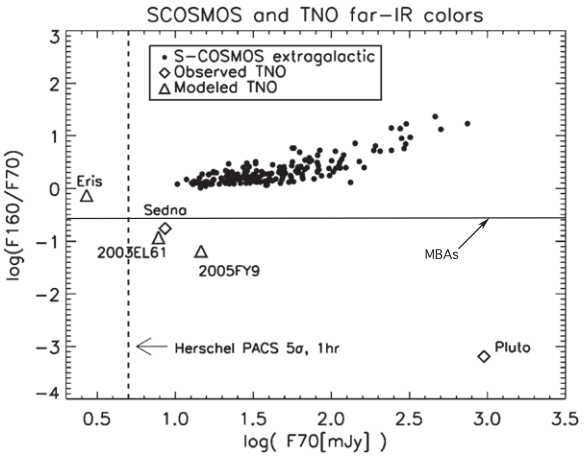

Figure 6. *Herschel* mission detection of MBAs and TNOs. The dots provide 160/70 μm color measurements from the *Spitzer* SCOSMOS catalogs. TNO observations for the three objects are obtained from Stansberry et al. (2008); the two modeled TNO colors are based on the STM. MBA colors and flux are obtained from Stansberry et al. (2008) and are designated by a horizontal, solid line. MBA F160/F70 color is approximately constant, though F70 will vary depending on asteroid size. NEOs are too faint in this wavelength region to be detected by *Herschel*.

5.3. Herschel MBAs, TNOs, and Background Objects

Objects in the outer solar system beyond the orbit of Neptune lie at temperatures $\lesssim$60 K and have thermal peak emission in the far-infrared at ~40–70 μm. At sufficient exposure depth, these objects are detectable by the *Herschel Space Observatory*. The PACS (Poglitsch et al. 2005; $5\sigma \sim 3$ mJy, 70 μm) and SPIRE (Griffin et al. 2005; $5\sigma \sim 1.8$ mJy, 250 μm) instruments are well suited to detect emission from colder, outer solar system bodies.

Figure 6 shows the measured far-infrared color of SCOSMOS sources at 70 and 160 μm in comparison to modeled and observed colors of a handful of TNOs. The region in color space where MBAs are present, as well as the *Herschel* PACS instrument sensitivity limit are noted by solid horizontal and dashed vertical lines, respectively. Note that *Herschel* wavelengths lie in the Rayleigh–Jeans tail for MBAs, making their 70/160 μm color comparable to the Sun's. Color-based identification of MBAs with *Herschel* may be feasible.

Stansberry et al. (2007) measured the 70 and 160 μm fluxes of 79 MBAs as part of the *Spitzer* MIPS calibration program. For main belt temperatures ~200 K, this wavelength region lies in the Rayleigh–Jeans thermal tail, where they found the F160/F70 ~ 0.265. The Stansberry et al. (2007) project measured brighter asteroids that are still detectable beyond their ~20 μm Wien peak, and F70 ranges from 0.189–21.511 Jy for their study. As temperatures of smaller MBAs should still be about 200 K because of their distance from the Sun, their F160/70 colors will also be ~0.265, though their F70 will be much lower. We have indicated the approximate location of MBAs in *Herschel* observations in the color space of Figure 6 using a solid horizontal line. These objects should be distinguishable from both extragalactic sources as well as TNOs, discussed below.

Far-infrared emission from TNOs is modeled assuming a spherical, non-rotating object, with emissivity and thermal inertia parameters of 0.9 and 0.756, using the STM as described in Section 4.2. Diameters and albedos have been obtained from JPL/Horizons, where available, or from the literature (Emery et al. 2007; Stansberry et al. 2008). As seen in Figure 6, the three populations, MBAs, TNOs, and extrasolar background sources, lie in distinct regions of color space, with decreasing flux in the wavelength region where *Herschel* operates. NEOs at this wavelength will exhibit a solar spectrum and their flux will fall below the *Herschel* PACS sensitivity limit of ~3 mJy for a 1 hr exposure.

Low proper motion objects in the outer solar system are more difficult to distinguish from background sources because of the relatively slow apparent rate of motion. Repeated exposures of the same field for the purpose of identifying TNOs need to be separated by several hours, as a best case scenario, for objects moving at 2″ hr^{-1}, assuming a pixel scale of 10″. As is the case for MBAs, the color of TNOs may provide a useful diagnostic tool to distinguish these relatively cold objects from background sources.

Table 6
Spitzer FLS-EPC Asteroid Flux in *WISE* Bandpasses

Asteroid	EcLat (deg)	$F_{\rm obs}$ 4.5 μm	$F_{\rm STM}$ 12 μm	$F_{\rm obs}$ 24 μm
7987 (1981 EV_{22})	0	0.04	11.85	13.79
9981 (1995 BS_3)	0	0.23	31.35	51.01
27168 (1999 AN_{21})	0	0.03	13.22	14.86
27293 (2000 AX_{136})	0	0.24	74.35	32.17
53273 (1999 FZ_{24})	0	0.24	10.91	15.65
79364 (1997 EU_4)	0	0.07	6.52	1.98
83004 (2001 QY_{160})	0	0.04	4.53	12.54
99307 (2001 SB_{182})	0	0.05	2.35	2.67
136040 (2002 WL_7)	0	0.10	5.52	24.35
2001 RP_{137}	0	0.02	1.09	3.13
2004 CA_{105}	0	0.34	7.75	6.28
49266 (1998 UW_5)	5	0.09	10.01	8.94
113186 (2002 RG_{106})	5	0.05	2.66	5.49
137958 (2000 CX_{18})	5	0.19	6.45	15.85
2004 EE_{58}	5	0.02	1.74	4.65

5.4. WISE NEOs and MBAs and Background Objects

WISE (Mainzer et al. 2005) is an all-sky survey at 3.3, 4.7, 12, and 23 μm, with sensitivities of 0.120, 0.160, 0.650, and 2.6 mJy, respectively. It is anticipated that the mission will detect thermal emission from a significant number of MBAs, as well as NEOs. *WISE* observes simultaneously in four bandpasses, making color determination possible for all objects detected. This survey returns to the same pointing 10–12 times over the course of 36 hr, which makes it possible to generate light curves for moving objects. The *WISE* team is committed to reporting their moving target observations to the Minor Planet Center within 10 days, to allow ground-based follow-up and the subsequent determination of albedo and radiometric diameter by combining ground-based optical and *WISE* infrared data.

While the primary means of detection exploits the relative motion of foreground objects between individual 47′ × 47′ frames, the color differences we note in Figure 4 may be used for verification or may be employed in situations where data quality issues hinder detection in adjacent spatial scans. In such cases, an individual frame may be examined for color differences between the different types of astronomical objects observed.

Since *WISE* employs a 12 μm detector, we have calculated the STM flux at this wavelength for the FLS-EPC asteroids (Table 6). We assume $p_v = 0.20$ as S-type asteroids are most prevalent. This table supplements the 12 μm STM flux with the observed flux at 4.5 and 24 μm, and we find the median $F(24/12) \sim 1.4$ and median $F(12/4.5) \sim 87$. Note that the 4.5

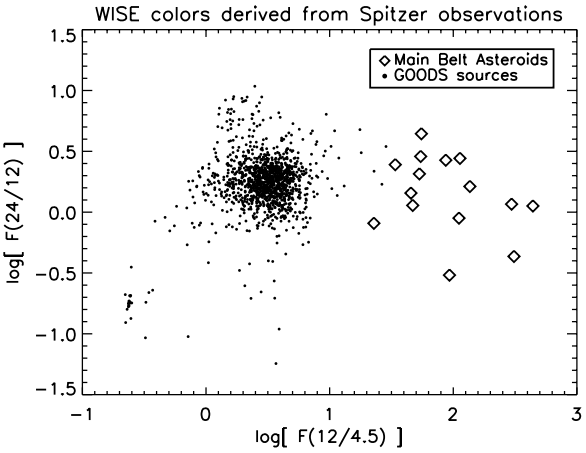

Figure 7. Modeled *WISE* 12 μm flux and observed *Spitzer* 4.5 and 24 μm flux are plotted in color–color space. FLS-EPC asteroids are plotted as diamonds, and stellar, galactic, and extragalactic sources are plotted as dots. At these wavelengths, asteroids move farther from background objects, down and to the right relative to their positions in Figures 3 and 4.

and 24 μm *Spitzer* observations are taken several hours apart and rotationally averaged for the shorter wavelength IRAC data as well as for some of the MIPS data. These median colors are based on a small sample size of modeled and observed flux, and the *WISE* mission will be able to provide more robust color values.

In Figure 7, we plot $F(24/12)$ versus $F(12/4.5)$ derived from Table 6. The region of color–color space occupied by *WISE* asteroids is farther from background objects, moving down and to the right in comparison to Figure 4. To obtain *Spitzer* 12 μm background object fluxes, we have looked at GOODS North and South (Dickinson et al. 2004) observations using the IRAC 8 μm channel as well as infrared spectrograph (IRS; Houck et al. 2004) taken at 15 μm. In the range 8–15 μm, extragalactic sources can either be red or blue, and the 12 μm flux can be approximated as the mean of the 8 and 15 μm measurements. This average value is more representative of the 12 μm flux than either the 8 or 15 μm bands individually. We have included the GOODS colors as solid dots, using IRAC 4.5 μm observations and MIPS 24 μm data. The colors presented in Figure 7 suggest that this technique will be even more effective to identify *WISE* asteroids, if uncertainties in all three bandpasses are small.

Verification of these results will be possible approximately six months after the end of the *WISE* cryogenic mission, when asteroid fluxes are released. At the time of this publication, only the astrometry of *WISE* solar system objects is available through the Minor Planet Center (http://www.cfa.harvard.edu/iau/mpc.html).

6. ASTEROID COLOR UNCERTAINTY

The purpose of the FLS-EPC was to detect as many faint asteroids as possible while covering as large an area of sky as possible. A consequence of this is that, given the asteroid size–frequency distribution, most of our detections are toward the faint end; with exposure time/pixel in the range 60–420 s pixel^{-1}, some of our observations have poor S/N (as low as S/N $\sim$ 2 for 0h) and cannot provide robust flux measurements. Although the range of colors of non-asteroidal sources spans about 2 orders of magnitude at IRAC wavelengths (Figure 3) and nearly 3 orders of magnitude at MIPS wavelengths (Figure 4), their color range generally lies away from the range of colors spanned by the asteroids. Hence, even though an individual asteroid's color may be uncertain by a factor of 2, this is still adequate for determining, with a fair degree of confidence, whether or not a given *Spitzer* source is likely to be an asteroid.

Flux variability due to asteroid rotation may contribute appreciably to color uncertainty, if multiband measurements are not simultaneous. IRAC's two FOVs each observe two wavelengths at the same time, so the colors presented in this study for 5.8/3.6 μm and 8.0/4.5 μm are not affected by rotational variability. This effect is more pronounced when considering 24/8.0 μm color, in Figure 4, as there was at least a 5 hr time spacing between 8 μm IRAC measurements and 24 μm MIPS measurements of the same asteroid.

As MBA rotation varies greatly, from a few minutes to tens of hours, and rotational periods for the FLS-EPC objects cannot be established without more observations, the level of uncertainty cannot be clearly established by this study. Missions such as *WISE*, with simultaneous measurements from 3.3 to 23 μm, will play a major role in characterizing MBA rotation periods. Once a large number of asteroids has been observed, it will be possible to constrain asteroid color more accurately, as a function of albedo and size.

7. CONCLUSIONS

Characterization of small MBA population is an ongoing process. The FLS-EPC has confirmed the significant role of thermal emission from asteroids in *Spitzer* data taken in and near the ecliptic plane. At the time these data were taken, the FLS-EPC survey increased the number of known asteroids in each field appreciably, by a factor of 2. Photometric measurements and comparison with STM fluxes using several albedo values suggests that the absolute magnitude for some known asteroids is overestimated and that typical diameters for our sample are in the 1–4 km range. A look at asteroid flux variation with wavelength in comparison to flux changes in other classes of astrophysical objects shows that asteroid colors are generally unique, though there may be some overlap due to measurement uncertainties for fainter asteroids with low S/N. Because of color uncertainties, this technique may provide statistical differentiation between object classes, but individual sources will require temporally separated observations to unambiguously identify them as moving, foreground objects. The nature of mid-IR asteroid SEDs may be exploited to generate color–color plots for these objects in comparison to stars, galaxies, and AGNs to identify an "asteroid box" where extrasolar sources are unlikely to be present. The FLS-EPC clearly demonstrates the need for additional multi-band mid-IR asteroid surveys not only for the purpose of characterizing MBAs, but also to enable observers to further distinguish between astrophysical sources and solar system objects in space-based infrared data.

In addition, *Spitzer* archival data may be exploited to look for asteroids and the results used to serve as ground work for asteroids observed by PanSTARRS, *WISE*, and *Herschel*. As *WISE* will observe a large number of asteroids, this mission's multiband observations may also be used to understand the variability of asteroid color as a function of diameter and albedo.

The authors acknowledge the late S. Tyler, whose enthusiastic presence is missed by the FLS-EPC team. During his years at the *Spitzer* Science Center, Mr. Tyler assisted in data analysis for this project. The authors also thank the anonymous referee

for helpful comments. B.B. thanks Dr. Tom Jarrett for providing valuable feedback, and the FLS-EPC team acknowledges Professor Jim Elliot for developing the original concept of the solar system First Look Survey. This work is based upon observations made with the *Spitzer Space Telescope*, operated by JPL, Caltech, and funded under NASA contract 1407. Additional work is funded by the NASA Herschel Science Center, operated by JPL, Caltech.

Facilities: *Spitzer* (IRAC, MIPS)

REFERENCES

Bottke, W. F., Jr., Vokrouhlický, D., Rubincam, D. P., & Nesvorný, D. 2006, Ann. Rev. Earth Planet. Sci., 34, 157
Bowell, E., et al. 1989, in Asteroids II (A90-27001 10-91), ed. R. P. Binzel, T. Gehrels, & M. S. Matthews (Tucson, AZ: Univ. Arizona Press), 549
dePater, I., & Lissauer, J. 2001, Planetary Sciences (Cambridge: Cambridge Univ. Press)
Dickinson, et al. 2004, ApJ, 600, L99
Emery, J. P., Dalle Ore, C. M., Cruikshank, D. P., Fernández, Y. R., Trilling, D. E., & Stansberry, J. A. 2007, A&A, 466, 395
Fazio, G. G., et al. 2004, ApJS, 154, 10
Fernández, Y. R., Jewitt, D., & Ziffer, J. E. 2009, AJ, 138, 240
Frayer, D. T., et al. 2009, AJ, 138, 1261
Granvik, M., et al. 2007, Icarus, 192, 475
Griffin, M. J., Swinyard, B. M., Vigroux, L., & Herschel-SPIRE Instrument Consortium Collaboration 2005, BAAS, 37, 1220
Harris, A. W. 1998, Icarus, 131, 291
Harris, A. W., Mueller, M., Lisse, C. M., & Cheng, A. F. 2009, Icarus, 199, 86
Houck, J. R., et al. 2004, ApJS, 154, 18
Juric, M., et al. 2002, AJ, 124, 1776
Lacy, M., et al. 2004, ApJS, 154, 166
Lebofsky, L. A., & Spencer, J. R. 1989, in Asteroids II (A90-27001 10-91), ed. R. P. Binzel, T. Gehrels, & M. S. Matthews (Tucson, AZ: Univ. Arizona Press), 128
Lebofsky, L. A., et al. 1986, Icarus, 68, 239
Lonsdale, C. J., et al. 2003, PASP, 115, 897
Mainzer, A. K., et al. 2005, Proc. SPIE, 5899, 262
Meadows, V. S., et al. 2004, ApJS, 154, 469
Mueller, T. G. 2002, Meteorit. Planet. Sci., 37, 1919
Mueller, M., Harris, A. W., & Fitzsimmons, A. 2007, Icarus, 187, 711
Parker, A., Ivezić, Ž, Jurić, M., Lupton, R., Sekora, M. D., & Kowalski, A. 2008, Icarus, 198, 138
Pilbratt, G. L., et al. 2010, A&A, 518, L1
Poglitsch, A., et al. 2005, BAAS, 37, 1219
Rieke, G., et al. 2004, ApJS, 154, 25
Romanishin, W., & Tegler, S. C. 2005, Icarus, 179, 523
Ryan, E. L., & Woodward, C. E. 2009, AJ, 137, 5134
Sanders, D. B., et al. 2007, ApJS, 172, 86
Stansberry, J. A., Grundy, W., Brown, M., Cruikshank, D., Spencer, J., Trilling, D., & Margot, J.-L. 2008, in The Solar System Beyond Neptune, ed. M. A. Barucci & H. Boehnhardt (Tucson, AZ: Univ. Arizona Press), 161
Stansberry, J. A., et al. 2007, PASP, 119, 1038
Stern, D., et al. 2005, ApJ, 631, 163
Tedesco, E. F., Cellino, A., & Zappalá, V. 2005, AJ, 126, 2869
Tedesco, E. F., & Dessert, F. 2002, AJ, 123, 2070
Tedesco, E. F., Veeder, G. J., Fowler, J. W., & Chillemi, J. R. 1992, The IRAS Minor Planet Survey, Final Report, Phillips Laboratory, Hanscom Air Force Base, MA
Trilling, D. E., et al. 2008, ApJ, 683, L199
Werner, M. W., et al. 2004, ApJS, 154, 1
Wolters, S. D., Green, S. F., McBride, N., & Davies, J. K. 2008, Icarus, 193, 535